PCCP

ROYAL SOCIETY OF CHEMISTRY

PAPER

Cite this: *Phys. Chem. Chem. Phys.*, 2024, **26**, 14713

Fast formation of anode-free Li–metal batteries by pulsed current

Katarina Cicvarić,[ab] Sebastian Pohlmann,[c] Bojing Zhang,[ab] Fuzhan Rahmanian,[ab] Leon Merker,[ab] Miran Gaberšček[d] and Helge Sören Stein*[abe]

Received 22nd February 2024,
Accepted 15th April 2024

DOI: 10.1039/d4cp00775a

rsc.li/pccp

Anode-free Li–metal batteries offer high energy density but are prone to dendrite formation during charging which can cause catastrophic failures. Ensuring dendrite-free smooth Li deposits during charging is therefore necessary. Suppressing dendrite growth can be achieved by pulsed current charging, especially during the formation cycle that largely determines the corrosion trajectory of a cell. As opposed to the constant-current technique, pulsed current techniques apply intermittently stopped current flows. This work investigates the electroplating of metallic Li onto a Cu foil current collector under constant-current and pulsed current formation protocols. In addition to smoother, less resistive electroplated metallic Li deposits and increased Coulombic efficiency, we show that by employing an optimized pulsed current formation protocol, the formation process is accelerated by a factor of 2 and the Coulombic efficiency was increased by 10% compared to a C/20 protocol. Finally, by employing a simple regression coupled to experimentation, we propose the pseudo-IR-drop to be used for live adjustment of pulsed current protocols *i.e.*, individually approach each cell at all SOC during formation.

Introduction

Lithium-ion batteries (LIBs) are dominating the markets of consumer electronics and electric vehicles[1,2] however, they cannot meet requirements in terms of energy density and research is ongoing to improve battery performance and decrease costs. Anode-free lithium–metal batteries (LMBs) are considered next-generation batteries as they promise high energy density. In the anode-free configuration, Li^+ ions are extracted from a cathode and electroplated as metallic Li onto a bare Cu foil current collector during charging, resulting in a Li–metal battery configuration, while during discharging, metallic Li is stripped from the Cu foil and intercalated back into the cathode. The absence of a Li-ion intercalation anode material enables thinner cells with lower weight, thus increasing both volumetric and gravimetric energy density, and reducing cost.[3–5] In addition, Li metal has the highest known theoretical specific capacity, low density and lowest absolute electrode potential.[6] However, during electroplating, Li metal tends to form irregular structures as Li nucleation occurs preferentially at energetically convenient sites. As electroplating proceeds, the nuclei continue to grow and their electric field increases attracting more Li ions from the electrolyte, forming a rough and porous Li film. This process is more pronounced by increasing electroplating current density. The excessive growth of irregular Li structures can lead to growth of Li whiskers dubbed "dendrites".[7–9] The rough and irregular metallic Li film has a high surface area in contact with the liquid organic electrolyte. Since Li metal can react with the organic solvents present in the electrolyte forming a well-known solid–electrolyte interface (SEI), the reaction leads to active Li loss which ultimately decreases the Coulombic efficiency. Furthermore, the needle-like dendrites can fall off the metallic Li film resulting in so-called "dead lithium" leading to further capacity loss. Even worse, extreme dendrite growth can pierce through the separator leading to a short-circuit of the cell and possibly a fire.[10,11] Drvarič Talian *et al.*[12] employed a transition line model describing the impedance response of metallic Li in contact with the electrolyte to study the dynamics of surface processes upon cycling. In this work, dendrites are divided into "live porous lithium" containing active lithium covered with SEI on the surface, and "dead porous lithium" at the electrolyte side containing passivated lithium consisting of SEI-like components electronically and ionically disconnected from the bulk active lithium. It is shown that as the thickness of dead lithium increases and the electrolyte dries out, the overall resistance of

[a] *Helmholtz Institute Ulm, Helmholtzstraße 1, 189081, Ulm, Germany. E-mail: katarina.cicvaric@tum.de, helge.stein@tum.de*
[b] *Karlsruhe Institute of Technology, Hermann-von-Helmholtz-Platz 1, 76344 Eggenstein-Leopoldshafen, Germany*
[c] *Bundeswehr University Munich, Department of Electrical Engineering, Werner-Heisenberg-Weg 39, 85577 Neubiberg, Germany*
[d] *National Institute of Chemistry, Department of Materials Chemistry, Hajdrihova ulica 19, 1000 Ljubljana, Slovenia*
[e] *Technical University of Munich, School of Natural Sciences, Department of Chemistry, Lichtenbergstr. 4, 85748 Garching bei München, Germany*

a cell increases significantly, which is a consequence of extensive lithium passivation.

To improve the performance of anode-free Li–metal batteries, several strategies have been suggested in the literature, such as: modification of the current collector, creation of artificial SEI, optimization of electrolyte formulations and modification of the cycling protocol.[3,4] Some of the work on current collector modification strategy includes investigation of other metals[13] and alloys,[14] or applying coatings such as lithophilic Ag nanoparticles[15] and SiOx[16] oxide layer which can improve Li wettability favouring more compact and uniform metallic Li deposits. Another approach is incorporating a Si_3N_4 nanoporous medium[17] or modifying Cu foil with C shells with Au nanoparticles[13] to suppress dendrite growth. Several reports propose 3D structured microporous Cu current collectors for promoting homogeneity of current distribution and hence preventing Li dendrite growth.[18] Artificial SEI formation strategy is realized by applying a protective coating onto the Cu surface, such as polyethylene oxide,[19] multilayer graphene,[20] and graphene oxide[21] which accommodate Li deposits and reduce Li surface passivation, or an Al_2O_3 layer[22] which improves the electrochemical stability of liquid electrolytes. Performance improvements were also attempted by modification of conventional carbonate-based electrolyte with 1 M $LiPF_6$, for instance, with dual salt LiDFOB/$LiBF_4$ liquid electrolyte,[23] dual additives KPF_6/Tris (trimethylsilyl) phosphite[24] and dual salt LiFSI/LiTFSI ether solution.[25] Modification of the cycling protocol strategy considers changing parameters such as cut-off voltages[26] or employing a pulsed current instead of constant-current charging.

Herein, we propose not to alter the chemistry but solely the electrochemical procedure to assess whether or not a first-order improvement can also be achieved. Pulsed current charging protocols can improve the performance of an anode-free Li–metal battery as it produces smoother and more compact electroplated films compared to constant current protocols. This has been demonstrated not only in LMB cycling[27–30] but also in the formation of an SEI on graphite,[31,32] and electroplating of various metals[33–35] and semiconductors.[36] During electroplating with constant current, the metal ions at the electrode surface are constantly consumed and their concentration decreases. As the plating proceeds, the constant consumption of metal ions leads to a depletion of ions at the electrode surface creating a concentration polarisation in the electrolyte where the Li^+ concentration in the bulk electrolyte is high and low at electrode surface. The higher the current density, the higher the rate of consumption of metal ions. The adsorbed metal ions are energetically unstable and tend to move towards already formed clusters, increasing the surface irregularities. In contrast to the constant-current protocol, the pulsed current consists of alternating constant current for a certain period of on-time, and off-time, during which the current density is 0. During the off-time, the concentration of metal ions at the electrode surface is being replenished, reducing the depletion layer. When the current is switched on again, the higher concentration of metal ions at the electrode surface hinders the mobility of the metal ions along the surface. Consequently, the deposits exhibit finer grains and a smoother surface as a result of reduced mobility of adsorbed ions at the electrode surface.[37,38]

Battery formation is an initial charge and discharge process in which a solid–electrolyte interface (SEI) layer is formed, typically on an anode. Conventionally, the formation is carried out for several charge and discharge cycles at very low currents such as C/20 taking days to complete.[39] In this work, we investigate the effects of constant current and pulsed current formation on the morphology and impedance of electroplated metallic Li on Cu foil current collectors in anode-free lithium–metal coin cells, as well as the Coulombic efficiency after formation. We show the difference in morphology of metallic Li electroplated at constant-current compared to that obtained with pulsed current charging, with smoother pulse-plated films exhibiting a lower resistance and a higher Coulombic efficiency. Furthermore, the time required to complete the formation cycle is more than halved by employing an optimised pulsed current formation protocol compared to the conventional constant-current C/20 protocol. The protocol is compatible with LIB manufacturing, and carried out without modifying the conventional chemistry, nor modifying the Cu current collector with additional material which adds weight and volume or an additional processing step of the Cu foil. In addition, by using a regression model, we propose the pseudo-IR-drop parameter as a potential control feature to further improve the Coulombic efficiency and reproducibility through a customized pulsed formation protocol.

Results and discussion

In this work 47 coin cells were formed by pulsed current charging and discharging at charging rates ranging from 1C to C/8, discharging rates ranging from 1C to C/16, on-times ranging from 0.25 s to 4 s, and off-time ranging from 0.75 s to 8 s. Although the main focus of this paper is on pulsed charging mechanism of metallic Li on Cu foil and the improvements it provides compared to constant-current charging, the experiments were carried showing that the pulsed current discharging is more beneficial compared to constant-current discharging. The Coulombic efficiency of C/2 pulsed current charging (t_{on} = 1 s, t_{off} = 3 s) and C/4 constant-current discharging is 0.49 ± 0.13, while that of C/2 pulsed current charging (t_{on} = 1 s, t_{off} = 3 s) and C/4 pulsed current discharging (t_{on} = 1 s, t_{off} = 3 s) is 0.64 ± 0.11. Therefore, the pulsed current protocols showed below were carried out by both pulsed current charging and discharging.

It has already been shown that at high constant-current discharging rates the capacity Li-ion batteries decreases.[40] In the case of discharge Li^+ ions intercalate back into the cathode, and the results indicate that reduction of concentration polarisation through pulsing could also improve the performance of discharging process. However, the mechanism of discharging is out the scope of this paper.

Surface morphology of electroplated metallic Li

To investigate morphology of metallic Li electroplated on a Cu foil current collector, constant-current (Fig. 1a) at C/20 and C/5,

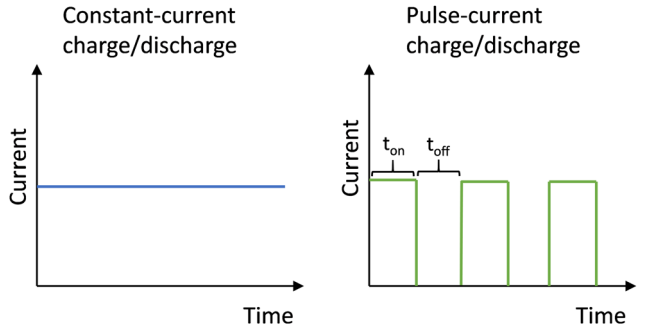

Fig. 1 Schematic representation of (a) constant current, and (b) pulsed current electroplating.

and pulsed current (Fig. 1b) at C/8 with on-time 1 s and off-time 2 s, and C/5 and C/2 both with on-time 0.25 s and off-time 0.75 s charging protocols were chosen for further investigation.

Fig. 2 shows scanning electron microscopy (SEM) micrographs of metallic Li electroplated at constant currents, C/20 (Fig. 2a and c) and C/5 (Fig. 2b and d).

As can be seen in the figures (Fig. 2a, b and 3a–c), metallic Li is electroplated as separate islands rather than continuous films, probably due to low Li content (cathode charge capacity approx. 0.2 mA h cm^{-2}). It can also be seen that the higher substrate coverage with smaller islands is achieved at high C/5 current (Fig. 2b) compared to low C/20 current (Fig. 2a). Furthermore, the morphology of the islands grown at low C/20 current (Fig. 2c) is smoother and the grains are more compact than at high C/5 current (Fig. 2d) with sharp, ''needle-like'' grains. Fig. 3 shows SEM micrographs of metallic Li electroplated at pulsed current C/8 with on-time of 1 s and off-time of 2 s (Fig. 3a and d), C/5 with on-time of 0.25 s and off-time of 0.75 s (Fig. 3b and e), and C/2 with on-time of 0.25 s and off-time of 0.75 s (Fig. 3c and f).

We observe an improvement of surface coverage by applying a higher current, with the highest current C/2 (Fig. 3c) producing the smallest and densest islands compared to C/5 and C/8 (Fig. 3b and a, respectively). This behaviour is in accordance with theory, as the nucleation rate is increased at higher current densities compared to lower current densities.[38] Comparing the morphology of the islands, C/5 and C/2 pulse-currents with millisecond pulses produce more compact, smoother, and larger ''rock-like'' grains (Fig. 3e and f, respectively), while C/8 with seconds-long pulses produce sharp, needle-like grains (Fig. 3d). Furthermore, comparing the morphology of pulsed C/5 and C/2 islands (Fig. 3e and f) with conventional constant-current C/20 charging (Fig. 2c), larger, smoother, and more compact grains are obtained with the pulsed charging protocol. The estimated number of Li monolayers per 0.25 s on-time is 0.16 and 0.05 for C/2 with t_{on} = 0.25 s, t_{off} = 0.75 s and C/5 with t_{on} = 0.25 s, t_{off} = 0.75 s protocols, respectively. The increase in deposited Li by approx. factor of 3 is expected as the current density applied in the C/2 protocol is approx. 3 times higher than in the C/5 protocol. For C/8 with t_{on} = 1 s, t_{off} = 2 s protocol the estimated number of monolayers per 1 s on-time is 0.08, which is close to the estimated value for C/5 with t_{on} = 0.25 s, t_{off} = 0.75 s. However, the longer off-time of 2 s could allow for surface diffusion and rearrangements of deposited Li leading to rough, ''needle-like'' morphology (Fig. 3d), which differs significantly from ''rock-like'' grains obtained by C/5 with t_{on} = 0.25 s, t_{off} = 0.75 s (Fig. 3e).

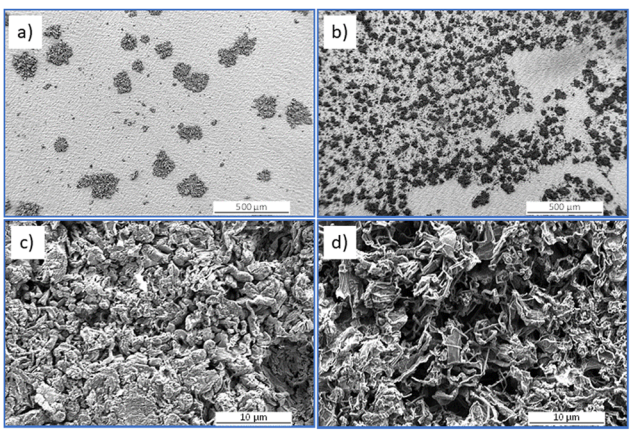

Fig. 2 SEM micrographs showing morphology of metallic Li after constant-current charging onto Cu foil current collector in anode-free Li–metal coin cell in 1 M $LiPF_6$ in ethylene carbonate : ethyl methyl carbonate (30 : 70 wt%) with 2 wt% vinyl carbonate electrolyte solution at C/20 (a) and (c) and C/5 (b) and (d). The magnification of micrographs is 100 times (a) and (b) and 5000 times (c) and (d).

Electrochemical impedance spectra of electroplated metallic Li

Fig. 4 shows electrochemical impedance spectra taken after Li electroplating onto Cu foil current collector (Fig. 4a) and the corresponding simplified equivalent electrochemical circuit (Fig. 4b). The latter was constructed based on a physical transmission line model for porous electrodes, in particular porous lithium electrode after cycling. The meaning of the simplified elements is as follows: R_1 represents the parallel resistance created by the movement of active ion (lithium ion) and counter charge in the separator under the external electric field. In the case of formation of the so-called dead lithium (porous inactive passive structures), R_1 also contains a contribution of migration of active and non-active charges in such ''dead'' porous system (ref. 12). R_2 can be approximated by:

$$R_2 = \sqrt{R_{par}R_{SEI}}\coth\sqrt{R_{par}/R_{SEI}} \quad (1)$$

where

$$R_{par} = \frac{R_{live1}R_{live2}}{R_{live1} + R_{live2}} \quad (2)$$

with R_{live1} and R_{live2} representing the transport of active (Li ion) and non-active ions, respectively, inside the pores of live Li dendrites (*i.e.* dendrites that still contain electronically connected metallic lithium). R_{SEI} denotes the transport resistance through the thin SEI film covering the live dendrites.[12] CPE1 can be considered as an approximation of the capacitive properties of the interface between electrolyte and live dendrites. The physical meaning of R_3 can be roughly described

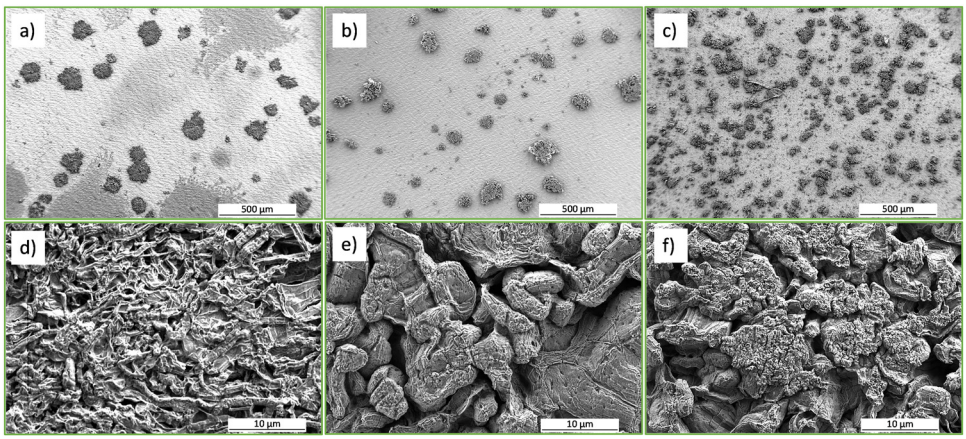

Fig. 3 SEM micrographs showing morphology of metallic Li after pulsed current charging onto Cu foil current collector in anode-free Li–metal coin cell in 1 M $LiPF_6$ in ethylene carbonate : ethyl methyl carbonate (30 : 70 wt%) with 2 wt% vinyl carbonate electrolyte solution at C/8 with t_{on} = 1 s, t_{off} = 2 s (a) and (d), C/5 with t_{on} = 0.25 s, t_{off} = 0.75 s (b) and (e) and C/2 with t_{on} = 0.25 s, t_{off} = 0.75 s (c) and (f). The magnification of micrographs is 100 times (a)–(c) and 5000 times (d)–(f).

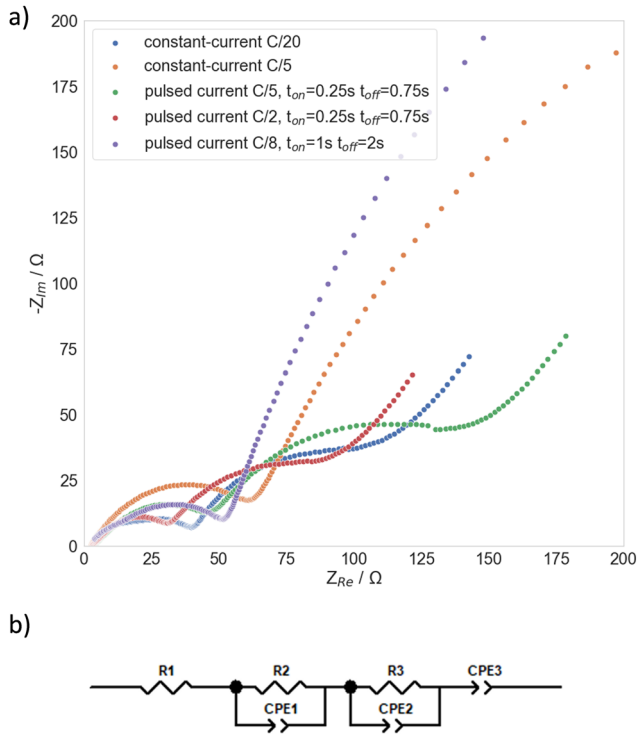

Fig. 4 Electrochemical impedance spectra of metallic Li electroplated onto Cu foil current collector in anode-free Li–metal coin cell in 1 M $LiPF_6$ in ethylene carbonate : ethyl methyl carbonate (30 : 70 wt) with 2 wt% vinyl carbonate electrolyte solution at different constant-current and pulsed current charging protocols (a) and an approximate equivalent electrochemical circuit derived from a general physics-based transmission line for porous lithium structures[12] (b).

with the following equation:

$$R_3 = \sqrt{R_{\text{live1}} R_{\text{SEI}}} \coth \sqrt{R_{\text{live1}} / R_{\text{SEI}}} \qquad (3)$$

CPE2 roughly corresponds to the chemical capacitance due to chemical diffusion of species in the pores of live dendrites. Finally, element CPE3 roughly replaces at least two further low-frequency diffusional phenomena, *i.e.* the chemical diffusion of mobile species in dead lithium (if present) and the chemical diffusion in porous separator (see ref. 12).

Table 1 shows the resistance values of electroplated metallic Li obtained at different constant-current and pulsed current protocols. The values of resistances were obtained by fitting the experimental data to the proposed simplified equivalent circuit (Fig. 4b). The lowest resistances are obtained by employing pulsed current C/2 with on-time of 0.25 s and off-time of 0.75 s, while the highest values are for Li electroplated with pulsed current C/8 with on-time of 1 s and off-time of 2 s. Moreover, Table 1 shows the average Coulombic efficiencies and sample standard deviations of three cells after the formation cycle, where both charging and discharging were carried out with the same constant-current or pulsed protocol. As can be seen from the table, the Coulombic efficiency decreases with increasing resistance, which is most evident for the constant-current C/5 and pulsed current C/8 t_{on} = 1 s, t_{off} = 2 s protocol. This is probably due to the increased roughness of electroplated Li, as can be seen from the SEM images (Fig. 2d and 3d). Consequently, rougher Li deposits have a larger surface area exposed to the solvent and form a passivated Li (SEI layer), resulting in increased resistance and higher active Li loss. In addition, the highly resistive, rough deposits obtained by pulsed current C/8 with on-time of 1 s and off-time of 2 s and with constant-current C/5 electroplating exhibit poor reproducibility, as indicated by the high standard deviation in Table 1. It should also be noted that a lot of cells formed under these conditions failed due to dendrite growth and the resulting short circuit. Conversely, the smoother deposits with lower resistance obtained by constant-current C/20, pulsed current C/5 and C/2 both with on-time of 0.25 s and off-time 0.75 s (Fig. 2c, 3e and f, respectively) exhibit significantly higher Coulombic efficiency and improved reproducibility. Importantly, using C/2 with on-time of 0.25 s and off-time of 0.75 s not only increased the Coulombic efficiency by

Table 1 Resistances obtained from fitting to equivalent electrochemical circuit and corresponding Coulombic efficiencies after formation process for various constant-current and pulsed current protocols

Formation protocol	R_2/Ω	R_3/Ω	Average Coulombic efficiency ± sample standard deviation
Constant-current C/20	38.8	54.4	0.73 ± 0.04
Constant-current C/5	55.2	321.4	0.65 ± 0.08
Pulsed current C/8 t_{on} = 1 s, t_{off} = 2 s	45.7	624.8	0.53 ± 0.14
Pulsed current C/5 t_{on} = 0.25 s, t_{off} = 0.75 s	45.2	83.1	0.73 ± 0.04
Pulsed current C/2 t_{on} = 0.25 s, t_{off} = 0.75 s	28.7	52.7	0.83 ± 0.04

approx. 10%, but also more than halved the time needed to carry out the formation compared to the conventionally used constant-current C/20 protocol.

Regression and descriptor

To find an appropriate combination of input parameters to further boost the analyzability of the Coulombic efficiency after formation, Gaussian process regression was used, considering the charge and discharge rate and the on- and off-time as input features and the Coulombic efficiency as output parameter. For this purpose, 47 coin cells were formed by pulsed charging and discharging at charging rates ranging from 1C to C/8, discharging rates ranging from 1C to C/16, on-times ranging from 0.25 s to 4 s, and off-time ranging from 0.75 s to 8 s with train-test split 80-20. Fig. 5a shows prediction results of the model with the loading settings as input yielding a rather low R^2 score of 0.53 on the testing data set.

The low R^2 score of 0.53 means that the fit is weak and that the model is not suitable for accurate predictions. The reason for this result is poor reproducibility of the output parameter if charge and discharge rate and on-time and off-time are used as input features. Further, the prediction of a continuous variable with, in this case, discontinuous input features deteriorates the results. Similarly, it has been observed experimentally that different pulsed protocols often produce the same or very similar Coulombic efficiencies, although on average certain pulsed protocols produce an improvement. In an attempt to find input parameters that could better explain the process and could therefore be used to predict Coulombic efficiency, the voltage curve was taken into consideration. More specifically, the voltage value at the end of current on-time and the voltage value at the beginning the current off-time which is the voltage(IR)-drop, and the voltage value at the end of current on-time and voltage value at the end of current off-time that encompasses the IR-drop and off-time, which we refer to as the pseudo-voltage(IR)-drop (Fig. 6). The reason for choosing the pseudo-IR-drop is to find a suitable off-time so not to keep the charging for too long to further reduce the time necessary for formation, but to keep it long enough for the replenishment of metal ions to occur in order to boost Coulombic efficiency. Multiple values of IR-drop and pseudo-IR-drop were taken as input parameters along charge and discharge curves, mainly at the points on the curves where the values change the most.

In this case, the Gaussian process regression model resulted in high R^2 values of 0.73 and 0.89 for IR-drop and pseudo-IR-drop testing data sets, respectively (Fig. 5b and c). This

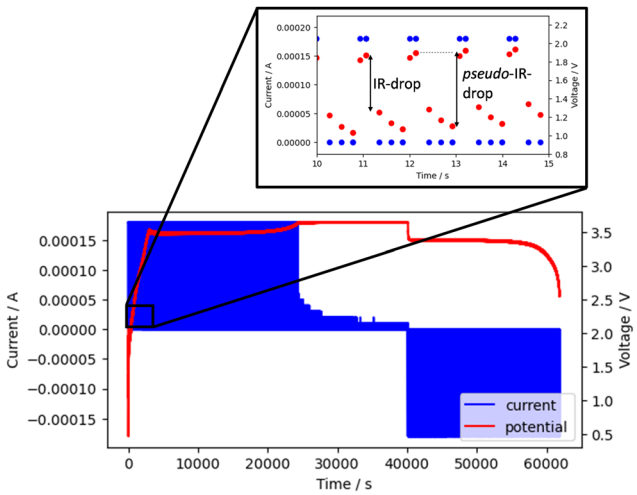

Fig. 6 Experimental pulsed current and voltage data of formation process in anode-free Li–metal coin cell in 1 M $LiPF_6$ in ethylene carbonate : ethyl methyl carbonate (30 : 70 wt) with 2 wt% vinyl carbonate electrolyte solution with IR-drop and pseudo-IR-drop representation.

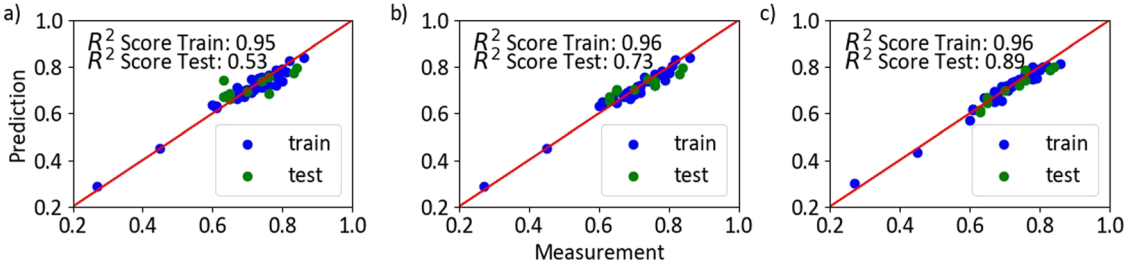

Fig. 5 Gaussian process regression predictions of Coulombic efficiency trained on pulsed current formation protocols in anode-free Li–metal coin cell in 1 M $LiPF_6$ in ethylene carbonate : ethyl methyl carbonate (30 : 70 wt) with 2 wt% vinyl carbonate electrolyte solution with charge rate, discharge rate, on-time and off-time as input features (a), IR-drop as input feature (b), and pseudo-IR-drop as input feature (c).

indicates that the fits are strong ($R^2 > 0.7$) and that the model predicts the dependent variable well, demonstrating the potential applicability of both IR-drop and pseudo-IR-drop as control parameters to achieve the desired Coulombic efficiency. It is likely that the high IR-drop corresponds to the formation of a rough metallic Li surface, since rough films possess higher resistances than smooth films, and could potentially be used to apply a reverse pulse to discharge dendrites. During the current off-time, it is possible that the mobility of Li ions along the surface allows for a rearrangement increasing somewhat the surface roughness. This could explain the significantly better prediction power of Gaussian process regression if pseudo-IR-drop is taken as input (R^2 = 0.89), compared to IR-drop (R^2 = 0.73). Hence, we hope that the IR-drop and pseudo-IR-drop could serve as a feedback loop to adjust the pulse magnitude/duration during charging to enable better control over Li electroplating and obtain smooth films. In this way, each cell could be treated individually with an appropriate procedure to boost capacity retention and reproducibility.

Conclusion

Metallic Li was electroplated onto a Cu foil current collector in an anode-free Li–metal coin cell by constant-current and pulsed current formation protocols. It is shown that smoother deposits can be obtained by using an optimised pulsed current protocol compared to constant-current protocols. After the complete formation cycle the obtained Coulombic efficiency of the optimised pulsed current formation C/2 with on-time of 0.25 s and off-time of 0.75 s protocol is approx. 10% higher than that of the conventional C/20 constant-current formation protocol. This is likely due to the obtained smoother metallic Li deposits with lower surface area and therefore less active Li loss due to the passivation reaction with the solvent. Moreover, the time necessary to complete the formation process is more than halved compared to the conventional, C/20 constant-current formation protocol. Furthermore, we show that reproducibility between the cells is poor, although on average the pulsed current formation protocol improves the Coulombic efficiency. This is confirmed using Gaussian process regression, which shows very weak agreement between predictions and test values if charge and discharge rate, and on and off-times are used as input features. A strong agreement between predictions and test values was achieved if IR-drop and pseudo-IR-drop were used as an input features. Hence, the Coulombic efficiency of the formation process could be explained and potentially predicted form IR-drop and pseudo-IR-drop by Gaussian process regression. Namely, the high IR-drop during pulsed charging is likely due to the formation of rough deposits and consequently the large surface area of the passivated Li, which has higher resistance than smooth Li deposits. The results show that the optimal pulse charging protocol has a high-current pulse which deposits large amount of Li but for a short time, before the region at the anode surface is depleted of Li^+ ions. The duration of the off-time should be long enough to allow the replenishment of Li^+ ion at the anode surface, but not too long so not to allow the rearrangement along the surface, which leads to increase in roughness. We joined IR-drop with off-time into pseudo-IR-drop in order to find an optimal off-time for metal ion replenishment. In this way, the pulsed current protocol could potentially be tailored to each cell individually, with appropriate off-time and/or reverse pulse to discharge the dendrites.

Materials and methods

Electrode preparation

Carbon-coated $LiFePO_4$ (LFP) powder, Super P conductive carbon black, and carboxymethyl cellulose were purchased from a commercial supplier AOT Battery, China. The materials were used for the preparation of cathode slurry as delivered. The cathode slurry was prepared by mixing $LiFePO_4$ powder, Super P conductive carbon black and 2 wt% carboxymethyl cellulose aqueous solution in wt% 85, 10 and 5, respectively. The slurry was mixed in centrifugal mixer (Thinky Mixer ARE-250, USA) at 2000 rpm for 10 minutes followed by defoaming at 400 rpm for 1 minute. The mixing procedure was then repeated again. Screen printing of the cathode slurry was carried out on 16 μm thick Al foil (AOT Battery, China) by doctor blade. The thickness of the coating was set to 50 μm and applied at 60 °C with a coating speed of 5 mm s^{-1}. The coatings were then dried overnight in an oven at 140 °C. Calendering of the coatings was carried out at 30 °C (MTI MSKH-RP-1A, China). The coatings were cut into 14 mm diameter disc using a disc puncher (AOT Battery, China) to serve as cathodes in coin cells. The cathodes were weighed prior to assembly to calculate specific capacity. A 9 μm thick copper foil (AOT Battery China) was cut with the disc puncher into 15 mm diameter discs that served as anodes. Polyester/Al-oxide sheet (Freudenberg performance materials) was cut into a 16 mm diameter disc that served as the separator. The prepared electrodes and separator were dried overnight 80 °C in an oven.

Coin cell assembly

The LFP|Cu electrodes were assembled into CR2032 coin-type cells in a nitrogen-filled glovebox (GS Glovebox Systemtechnik, Germany). To facilitate the reproducibility and productivity of cell assembly, an in-house developed robotic cell assembly system AutoBASS was employed for the massive cell manufacturing. Detailed AutoBASS coin cell assembly procedure is described in Zhang *et al.*[41] Prior to assembly the coin cell parts (Pi-KEM, UK) were washed in an ultrasonic bath filled with isopropanol and left to dried in an oven at 80 °C overnight. Pick and stack of the cell components were accomplished by a 6-axis robotic arm (Mecademic, Canada) with a linear motor axis (Jenny Science, Switzerland). Dispersing of electrolyte was completed by a second robot with an automatic liquid handling dispenser (Sartorius AG, Germany). Automatic sealing of the cells was done by the digital electric crimper (MTI, USA) modified with a microcontroller. As an electrolyte 35 μl of

1 M $LiPF_6$ in ethylene carbonate : ethyl methyl carbonate (30 : 70 wt%) with 2 wt% vinyl carbonate electrolyte (E-lyte, Germany) was added per coin cell. The cells were stored with anode side facing down for wetting for at least 24 h prior to electrochemical experiments.

Electrochemical experiments

Charge and discharge experiments were carried on LFP|Cu coin cell out using an Arbin battery tester under atmospheric conditions. Electrochemical impedance spectroscopy measurements were carried out after the first charge cycle using the PalmSens4 potentiostat/galvanostat in the frequency range of 1 MHz to 0.1 Hz with an amplitude voltage of 10 mV.

Morphology analysis

Prior to morphology analysis, coin cells were disassembled with a crimper (MTI MSK-160E, China) inside a glovebox and the anode was rinsed with EMC. The Li anode was transferred into scanning electron microscope (Thermo Fisher Scientific, USA) for surface morphology examination. The scanning electron microscopy images were taken at 2 kV acceleration voltage.

Data availability

The raw data is available at **https://zenodo.org/records/8276087** under the DOI 10.5281/zenodo.8276087 as well as the analysis code used to generate the figures.

Conflicts of interest

There are no conflicts to declare.

Acknowledgements

This work contributes to TUM.Battery, the Munich Data Science Institute, and the Munich Institute for Robotic and Machine Intelligence. This work contributes to the research performed at CELEST (Center for Electrochemical Energy Storage Ulm-Karlsruhe). This project also received funding from the European Union's Horizon 2020 research and innovation program under grant agreement No 957189. The project is part of BATTERY 2030+, the large-scale European research initiative for inventing sustainable batteries for the future, funded by European Union's Horizon 2020 research and innovation program under Grant Agreement No. 957213 (BIG-MAP).

References

1 G. Zubi, R. Dufo-López, M. Carvalho and G. Pasaoglu, *Renewable Sustainable Energy Rev.*, 2018, **89**, 292–308.
2 A. Manthiram, *ACS Cent. Sci.*, 2017, **3**, 1063–1069.
3 C. Heubner, S. Maletti, H. Auer, J. Hüttl, K. Voigt, O. Lohrberg, K. Nikolowski, M. Partsch and A. Michaelis, *Adv. Funct. Mater.*, 2021, **31**, 2106608.
4 R. V. Salvatierra, W. Chen and J. M. Tour, *Adv. Energy Sustainability Res.*, 2021, **2**, 2000110.
5 J. Qian, B. D. Adams, J. Zheng, W. Xu, W. A. Henderson, J. Wang, M. E. Bowden, S. Xu, J. Hu and J. G. Zhang, *Adv. Funct. Mater.*, 2016, **26**, 7094–7102.
6 L. A. Selis and J. M. Seminario, *RSC Adv.*, 2019, **9**, 27835–27848.
7 S. Li, Z. Luo, L. Li, J. Hu, G. Zou, H. Hou and X. Ji, *Energy Storage Mater.*, 2020, **32**, 306–319.
8 T. Fuchs, J. Becker, C. G. Haslam, C. Lerch, J. Sakamoto, F. H. Richter and J. Janek, *Adv. Energy Mater.*, 2023, **13**, 2203174.
9 B. Thirumalraj, T. T. Hagos, C. J. Huang, M. A. Teshager, J. H. Cheng, W. N. Su and B. J. Hwang, *J. Am. Chem. Soc.*, 2019, **141**, 18612–18623.
10 Z. Xie, Z. Wu, X. An, X. Yue, J. Wang, A. Abudula and G. Guan, *Energy Storage Mater.*, 2020, **32**, 386–401.
11 K. Liu, Y. Liu, D. Lin, A. Pei and Y. Cui, *Sci. Adv.*, 2018, **4**, eaas9820.
12 S. Drvarič Talian, J. Bobnar, A. R. Sinigoj, I. Humar and M. Gaberščček, *J. Phys. Chem. C*, 2019, **123**, 27997–28007.
13 K. Yan, Z. Lu, H. W. Lee, F. Xiong, P. C. Hsu, Y. Li, J. Zhao, S. Chu and Y. Cui, *Nat. Energy*, 2016, **1**, 16010.
14 V. Pande and V. Viswanathan, *ACS Energy Lett.*, 2019, **4**, 2952–2959.
15 S. Cui, P. Zhai, W. Yang, Y. Wei, J. Xiao, L. Deng and Y. Gong, *Small*, 2020, 1905620.
16 W. Chen, R. V. Salvatierra, M. Ren, J. Chen, M. G. Stanford and J. M. Tour, *Adv. Mater.*, 2020, 2002850.
17 N. Li, W. Wei, K. Xie, J. Tan, L. Zhang, X. Luo, K. Yuan, Q. Song, H. Li, C. Shen, E. M. Ryan, L. Liu and B. Wei, *Nano Lett.*, 2018, **18**, 2067–2073.
18 M. Kurniawan and S. Ivanov, *Energies*, 2023, **16**, 4933.
19 A. A. Assegie, J. H. Cheng, L. M. Kuo, W. N. Su and B. J. Hwang, *Nanoscale*, 2018, **10**, 6125–6138.
20 A. A. Assegie, C. C. Chung, M. C. Tsai, W. N. Su, C. W. Chen and B. J. Hwang, *Nanoscale*, 2019, **11**, 2710–2720.
21 Z. T. Wondimkun, T. T. Beyene, M. A. Weret, N. A. Sahalie, C. J. Huang, B. Thirumalraj, B. A. Jote, D. Wang, W. N. Su, C. H. Wang, G. Brunklaus, M. Winter and B. J. Hwang, *J. Power Sources*, 2020, **450**, 227589.
22 Z. Tu, M. J. Zachman, S. Choudhury, K. A. Khan, Q. Zhao, L. F. Kourkoutis and L. A. Archer, *Chem. Mater.*, 2018, **30**, 5655–5662.
23 R. Weber, M. Genovese, A. J. Louli, S. Hames, C. Martin, I. G. Hill and J. R. Dahn, *Nat. Energy*, 2019, **4**, 683–689.
24 T. M. Hagos, G. B. Berhe, T. T. Hagos, H. K. Bezabh, L. H. Abrha, T. T. Beyene, C. J. Huang, Y. W. Yang, W. N. Su, H. Dai and B. J. Hwang, *Electrochim. Acta*, 2019, **316**, 52–59.
25 T. T. Beyene, H. K. Bezabh, M. A. Weret, T. M. Hagos, C.-J. Huang, C.-H. Wang, W.-N. Su, H. Dai and B.-J. Hwang, *J. Electrochem. Soc.*, 2019, **166**, A1501–A1509.
26 M. Genovese, A. J. Louli, R. Weber, S. Hames and J. R. Dahn, *J. Electrochem. Soc.*, 2018, **165**, A3321–A3325.
27 G. García, S. Dieckhöfer, W. Schuhmann and E. Ventosa, *J. Mater. Chem. A*, 2018, **6**, 4746–4751.

28 J. Zhang, Z. Zhou, Y. Wang, Q. Chen, G. Hou and Y. Tang, *ACS Appl. Mater. Interfaces*, 2022, **14**, 50414–50423.
29 H. Yang, E. O. Fey, B. D. Trimm, N. Dimitrov and M. S. Whittingham, *J. Power Sources*, 2014, **272**, 900–908.
30 Q. Li, S. Tan, L. Li, Y. Lu and Y. He, *Sci. Adv.*, 2017, **3**, e1701246.
31 F. M. Wang, H. Y. Wang, M. H. Yu, Y. J. Hsiao and Y. Tsai, *J. Power Sources*, 2011, **196**, 10395–10400.
32 F. M. Wang, J. C. Wang and J. Rick, *Electrochim. Acta*, 2014, **147**, 582–588.
33 G. Garcia, E. Ventosa and W. Schuhmann, *ACS Appl. Mater. Interfaces*, 2017, **9**, 18691–18698.
34 C. Y. Chen, M. Yoshiba, T. Nagoshi, T. F. M. Chang, D. Yamane, K. Machida, K. Masu and M. Sone, *Electrochem. Commun.*, 2016, **67**, 51–54.
35 J. B. Marro, T. Darroudi, C. A. Okoro, Y. S. Obeng and K. C. Richardson, *Thin Solid Films*, 2017, **621**, 91–97.
36 K. Cicvarić, L. Meng, D. W. Newbrook, R. Huang, S. Ye, W. Zhang, A. L. Hector, G. Reid, P. N. Bartlett and C. H. K. de Groot, *ACS Omega*, 2020, **5**, 14679–14688.
37 X. Sun, X. Zhang, Q. Ma, X. Guan, W. Wang and J. Luo, *Angew. Chem., Int. Ed.*, 2020, **59**, 6665–6674.
38 M. Schlesinger and M. Paunovic, *Modern Electroplating*, John Wiley & Sons, Inc., 4th edn, 2000.
39 Y. Liu, R. Zhang, J. Wang and Y. Wang, *iScience*, 2021, **24**, 102332.
40 G. Ning, B. Haran and B. N. Popov, *J. Power Sources*, 2003, **117**, 160–169.
41 B. Zhang, L. Merker, A. Sanin and H. S. Stein, *Digital Discovery*, 2022, **1**, 755–762.

